SSRG International Journal of Mechanical Engineering
ISSN: 2348-8360/ https://doi.org/10.14445/23488360/IJME-V13I9P106

Volume 13 Issue 9, 89-106, September 2026

Original Article

Low-Frequency Magnetic Field Mitigation Using Recyclable Sintered Pure-Iron Powder Compacts for Safer Power and Sensor Infrastructure

Viraj Barge[1], Nitin Satpute[2], Mukund Kulkarni [3]

[1,2]Department of Mechanical Engineering, Vishwakarma University, Maharashtra, India.
[3] Department of Computer Science and Engineering, Vishwakarma University, Maharashtra, India.

[2]Corresponding author : nitin.satpute@vupune.ac.in

Received: 12 June 2026 Revised: 04 Septmber 2026 Accepted: 18 September 2026 Published: 26 September 2026

Abstract *- High-current carrying conductors, electrical machines, power-electronic systems, and sensors generate low-frequency magnetic fields that can cause electromagnetic interference and may result in higher magnetic-field exposure in occupied or sensitive environments. This study proposes a new low frequency shielding material in the form of sintered pure-iron powder compacts as an alternative to the conventional high-permeability magnetic shielding alloys. This material is manufactured by following controlled environment annealing, green compaction and sintering of high purity iron powder. The magnetic properties of the compacted specimen were determined by characterization according to IEC 60404-4 standard, and scanning electron microscopy was used to study the microstructural features, and chemical analysis was performed by using energy dispersive spectroscopy to validate purity of the iron powder. Experimentally determined magnetic properties were used in finite element simulations to evaluate the shielding performance when different shielding geometries manufactured from the proposed material are placed around a current-carrying conductor. Analysis was done when the conductor carries current of 1000 Amp with focus to evaluate different shielding topologies, including open, square, hexagonal and circular shapes. Analysis indicated that the circular closed-shielding geometry can achieve better shielding effectiveness by ensuring a low-reluctance flow path for magnetic-flux shunting. Finite element simulation results indicated that the proposed pure-iron compact based shielding can ensure shielding effectiveness of 12.6 dB, as compared with 13.35 dB for Mu-metal and 11.24dB for Fe–Si steel. There will be 79% attenuation of the magnetic field at radial distance of 1 m from the conductor with use of the proposed shielding material. The proposed material has several sustainability advantages beyond providing shielding performance, which includes use of recyclable pure iron, reduced dependence on expensive Ni-based alloys, geometry flexibility, and repairability. The proposed material can provide safer, reliable, and more sustainable low-frequency magnetic shielding for use in power infrastructure, sensor systems, medical instrumentation, electric vehicle modules, and industrial equipment.*

Keywords *- Low-frequency magnetic shielding, Sustainable shielding material, Sintered pure iron, Magnetic field attenuation, Recyclable magnetic material.*

1. Introduction

Stray magnetic field generated by current-carrying conductors and electrical devices can adversely affect nearby sensors and actuators. In particular, a low-frequency magnetic field originated from conductors carrying high current poses a risk to human life in case of long exposure, in addition to causing faulty performance by sensitive electronic equipment. Therefore, use of low-frequency magnetic shielding is becoming more important in the modern electrified infrastructure, where current-carrying conductors, electric-drive systems, power-electronic converters, electric vehicle modules, medical instruments, and industrial sensing systems are used. In case of these devices, magnetic shielding has become a functional requirement as well as a sustainability issue. An effective and sustainable low frequency shielding can deliver a safer electrical infrastructure, reliable sensor working, better reliability and life of the equipment, in addition to avoiding the use of expensive and difficult-to-recycle shielding alloys. Conventional magnetic shielding materials include thick sheets of pure iron, Fe-Si, Mu-metal, and other alloys. These materials are expensive and have additional limitations of heavy and bulky construction, with limited adaptability to complex geometries, and fabrication difficulties. Further, the manufacturing process involves plastic deformation, resulting in internal stresses that adversely affect magnetic properties. Electromagnetic shielding materials are developed according to the magnetic field frequencies, where the mechanism used for shielding includes magnetic flux diversion by providing a low reluctance path. When the frequency of shielding is low (DC to 1 kHz), high-permeability materials like pure iron, Mu-metal, Permalloy and silicon steel are generally employed because these materials have the ability to divert the magnetic flux due to high permeability [1]. High frequency radio shielding applications use metals like copper, aluminum and custom conductive composites because of their high electrical conductivity and ability to redirect high frequency electromagnetic fields [2]. The selection of material for magnetic shielding applications is based on various considerations such as Shielding Effectiveness achieved (SE), permeability, magnetic field saturation limit, and application requirements. Yeh et al. [3] manufactured a Soft Magnetic Composite (SMC) material with FeCoNiSiCuNb alloy, which has 22.8 emu/g of saturation magnetization limit, and the material demonstrated the coupling coefficient of 0.84 as compared to conventional shielding materials. A passive magnetic shield composed of iron-based nanocrystalline material has low magnetic noise [4]. Authors have reported the simulation results when a cylindrical-shaped geometry having aspect ratios of 1.3 and 1.4 is used for radial and axial direction magnetic shielding. Jing et al. [5] reported theoretical simulation results for magnetic shielding performance evaluation of a double-layered planar structure when used for shielding a circular loop magnetic field.

Authors have reported effects of different design parameters, including material type, shielding layer thickness, and interlayer spacing on the SE when different materials, including aluminum, low-carbon steel, and permalloy is used in the construction. Li et al. investigated the application of selective laser melting for manufacturing Ni-15Fe-5Mo Permalloy for magnetic shielding applications. Authors have reported that the optimized SLM process resulted in a relative density of 99.86%, while the subsequent annealing operation improved the magnetic characteristics of the material, resulting in a saturation magnetization of 78 emu/g [6]. Gohil et al. [7] used soft iron for low frequency magnetic shielding, where the material has a maximum permeability of 3500-8000 and saturation magnetic induction of 2.15 T. Ji and Sun presented a progressive loss decomposition technique for soft magnetic materials used in low-frequency magnetic shielding. Authors have studied hysteresis loss, eddy current loss, and excess loss to facilitate accurate prediction of the characteristics of shielding materials [8]. Recent studies have reported shielding material manufactured using porous structures, conductive and magnetic nanoparticles, carbon nanotubes, MXenes polymer foams, and hydrogels [9 - 12]. The reported work is primarily designed for high-frequency applications and has nanostructured constituents that require a costly and complicated manufacturing process, limiting their large-scale affordability.

Inductive sensors' performance may be impacted by possible ElectroMagnetic Interference (EMI) from power lines, electrical equipment, and geomagnetic field changes, leading to measurement inaccuracies. To ensure these sensors perform accurate measurements, effective magnetic shielding is crucial. Magnetic shielding minimizes the effect of disturbances caused by external magnetic fields, which is necessary for reliable operation, which is particularly important for critical applications such as biomedical and precision measurement systems. Yang et al. developed a magnetic shielding geometry to minimize undesirable effect of stray magnetic field on a current sensor measurement. Authors evaluated the SE using Finite Element Modelling (FEM) with the use of coil winding and permanent magnets for originating the external disturbing magnetic field.

Authors have reported a maximum error of 0.8% in estimating the SE for frequencies up to 200 kHz [13]. Ruban et al. discussed the application of magnetic shielding to a Hall-effect current sensor where the shielding material was manufactured from thin silicon steel sheets, where the shielding performance is evaluated for maximum current up to 720 A [14]. Liu et al. presented eddy-current sensor incorporated with enhanced magnetic shielding. The experiments demonstrated that the sensor identified notch defects at a depth of 7 mm in a stainless-steel plate using a 1 kHz harmonic excitation, with better accuracy than the unshielded sensor [15]. Mirzaei et al. developed a ferromagnetic shielding for a speed sensor to achieve improved sensitivity and better accuracy, with external disturbing magnetic field presence. Experiments were conducted on rotating disks made of aluminum and iron, where the sensor revealed sensitivities of 110 μV/m/s at 300 Hz for iron and 0.21 mV/m/s at 120 Hz for aluminum, while exhibiting a maximum linearity error of 0.26% [16]. Vasić et al. developed an analytical model for a ferrite-cored eddy-current sensor surrounded by a magnetic shield and evaluated its performance over the frequency range of 5–100 kHz [17]. Zhou et al. reported a canister-shaped pulsed eddy current sensor fitted with shielding and revealed that the shielding ensures enhanced defect detection in contrast to sensors operated without shielding [18]. The reported studies have investigated application-specific individual sensor shielding configuration and there is a need to design a general purpose, recyclable, and geometry-flexible shielding material that can be used for diverse sensor systems.From a sustainability point of view, an effective magnetic shield around sensors is essential for the reliability and lifespan of measurement systems in energy, mobility, healthcare, manufacturing and condition monitoring applications. Sensors based on magnetic-field sensing and electromagnetic induction, such as Hall-effect current sensors, eddy-current sensors, magnetic position sensors, and biomedical instrumentation, exhibit drift, false readings, decreased sensitivity or failure when subjected to low-frequency magnetic interference. The magnetic shield minimizes the impact of the outside magnetic field, enhances operational safety, and facilitates reliable measurement.

Dang et al. studied electromagnetic shielding for a reaction wheel assembly, where the authors achieved a reduction in the stray magnetic field by up to 75% at 1 m distance [19]. Zhu et al. fabricated stretchable magnetic liquid-metal films for wearable electromagnetic shielding and sensing applications. The films achieved a specific shielding effectiveness of 404 dB mm^{-1} at 400% strain, while also exhibiting strain-sensitive conductivity and wireless human-motion detection capability [20]. Hou et al. developed low-reflective electromagnetic shielding materials utilizing 3D-printed PLA@MWCNT and PDMS@CIP composites. These materials achieved SE of 31 dB, which can be used for electromagnetic wave protection devices [21]. Victoria et al. [22] improved the performance of a near-field communication system using ferrite-polymer composite shielding material to ensure improved communication performance in the presence of nearby conductive surfaces and associated stray magnetic fields.

Yoo and Lee proposed Fe-based amorphous soft magnetic sheets combined with a flexible conductive sheet for electromagnetic shielding within the 1 kHz to 10 GHz frequency range, where a triple-sandwich structure achieved an SE of 80 dB [23]. Wodey et al. introduced a scalable design for magnetic shielding of a very-long-baseline atom interferometry device. Authors used a high-permeability Ni–Fe alloy (permalloy) in the 10 m long shielding structure to achieve residual magnetic fields lower than 4 nT and longitudinal inhomogeneities below 2.5 nT/m over the central 8 m of the shielded region [24]. Zhang et al. proposed a wireless power transfer system for electric vehicles that utilizes dual transmitting coils along with a ring-series magnetic shielding coil [25]. Han et al. introduced a flexible and ultrathin electromagnetic shielding film made with cellulose nanofiber and nickel-coated graphene (TRGO@Ni).

Authors used 50 wt% filler loading and vacuum filtration to achieve an SE of 32.2 dB, when the material conductivity was 262.7 S/m [26]. Peymanfar et al. investigated the effects of particle size and polymer medium on the magnetic and electromagnetic shielding performance of $CuCo_2S_4$ nanoparticle-based composites [27]. Henaish et al. investigated the use of Ni-Cu-Mg-Zn ferrite nanomaterials manufactured using flash auto-combustion. It was observed that increasing the Mg content lowers crystal development, increases the Curie temperature, and diminishes mass attenuation and effective atomic number, which influences shielding performance [28]. He et al. prepared Polydimethylsiloxane (PDMS)-based composite materials with multi-walled carbon nanotubes, Ni, and Sb_2O_3 fillers for improved electromagnetic interference shielding performance. The symmetric laminated structure exhibited an SE of approximately 57.4 dB with an absorption coefficient of approximately 0.75, along with enhanced impedance matching and diminished microwave reflection [29].

Shi et al. discussed a 3D-printed graphene–carbon nanotube-based material for magnetic shielding application, that can be integrated directly in the electronic components and achieve SE of up to 61.4 dB [30]. Lv et al. proposed a periodic porous carbon nano tube-based shielding metamaterial manufactured with use of fused-deposition modelling. Authors established a correlation between pore geometry, size, orientation, and material thickness with SE [31]. The optimized structures ensured a maximum SE of 95 dB and a maximum value of absorption coefficient at 0.83. Rajan et al. developed a hybrid material for magnetic shielding manufactured by using electrically conductive carbonized cotton and magnetic ferrite particles [32]. Ferrite material reduced electromagnetic reflection and improved absorption of the magnetic field, leading to 60 dB of SE. Although these advanced composite and additively manufactured materials provide high SE, structural customizability, and multifunctionality, these materials are primarily designed for high-frequency electromagnetic interference and generally require hybrid nanofillers or a complex and costly manufacturing process.

Mu-metal and Permalloy have higher magnetic permeability and are widely used for low-frequency shielding. These materials have limitations in their broader use in sustainable engineering applications due to high cost, low mechanical strength, lower corrosion resistance, lower creep strength, dependence on Ni-rich materials, limited availability in standard sheet or ribbon forms, and difficulties in fabricating thick or three-dimensional shielding geometries [33, 34]. In addition complex alloy compositions, specialized heat-treatment requirements, complicated repair, reuse and recycling difficulties are further limitations. Magnetic saturation flux density of these materials is limited to 1.0 T, and these can be used up to 400°C [35, 36]. There are attempts to use an alloy of Fe, Bo, Si and other elements with sandwich structures having a few conducting layers for electromagnetic shields. These high-permeable alloys reported in the literature have limitations of high material and processing costs.

Further, these materials are very brittle, have poor machinability, and the complicated recycling route due to the presence of certain alloying elements, which are hazardous for the environment. Attempts have been made to use pure iron for electromagnetic field attenuation, where the material is manufactured using conventional and modified pyrometallurgical processes. These manufacturing methods have difficulties in controlling impurities and oxidation during processing, which necessitate complex and costly process controls [37, 38]. Gohil et al. [7] used soft iron in cylindrical shaped geometry for low-frequency magnetic-field attenuation; however, conventional sheet-based shielding geometry has limited geometric flexibility and necessitates additional forming operations for fabrication of complex three-dimensional structures.

This makes this material more suitable for planar or laminated magnetic shielding geometry. Furthermore, the rolling and annealing processes are complex and expensive, therefore the foil-shaped material is not scalable for 3-dimensional geometries.

Literature review highlights substantial developments in development of high-permeability alloys, multilayer structures, nanocomposites, polymer-based materials, and customized shielding geometries for magnetic shielding. However, most of the studies are applicable for high-frequency shielding and are associated with high-cost material, specialized heat treatment, costly and complex processing. The available low-frequency shielding material is manufactured in planar sheets, ribbons, or cylindrical form. This limits application of the shielding material to different 3-dimensional geometries. Further, there are concerns about lower saturation flux density, cost, structural robustness, recyclability, scalable manufacturing, and geometric flexibility. Therefore, there is an unmet need to develop iron-based, economical and near-neat-shaped shielding material that can be applied to complex three-dimensional geometries for application across a broad range of low-frequency magnetic shielding applications. This kind of shielding material is crucial for power networks, transportation systems, sensor-driven automation, and health-sensitive infrastructure.

The present work is motivated to overcome the above-mentioned limitations and develop a low-frequency magnetic shielding material using a resource efficient high purity pure-iron powder. The proposed manufacturing process includes controlled-environment annealing, green compaction and sintering to prepare mechanically strong shielding compacts with the desired geometry. The material properties are characterized by DC magnetic testing according to IEC 60404-4, Energy Dispersive Spectroscopy (EDS) and Scanning Electron Microscopy (SEM). Magnetic properties are determined from experimentation are used in finite element simulations for magnetic shielding applied around a conductor with 1 kA current. The open and closed shielding configurations are compared, and the impact of the geometry as well as the thickness of the shielding material is investigated. The sustainability aspect of the present work is the development of a pure-iron-based, near-neat-shaped manufacturable, low-dependence on expensive high-permeability alloys, repairable shielding structures with geometric flexibility, which could be utilized in safer power infrastructure and reliable low-frequency sensor systems.

2. Materials and Methods

Industrial Metal Powder Pvt. Ltd., Pune, made electrolytic iron powder is used in the present work. Particle size distribution was estimated from SEM micrographs using image-based analysis (Make: Zeiss, Germany, Model: Sigma HV). The electrolytic iron powder exhibits an irregular morphology with a median particle size (D50) of approximately 74 µm, while the D10 and D90 particle sizes were 28 µm and 135 µm, respectively. The powder is hereafter referred to as Fe74 in the further sections. Figure 1 shows the SEM image of particles, which reveals that the Fe74 powder has a broader particle size distribution with irregular and angular particle shapes. This powder morphology is achieved through the powder production method using electrode deposition, followed by a ball milling operation. The manufacturing route followed for this powder offers the advantage of high purity (>99.8%) [39, 40]. Furthermore, the selected powder has a broad particle size distribution with coarse and fine particles, that can contribute to superior particle packing during the compaction process. Small particles effectively fill the interstitial spaces between the big sized particles, resulting in higher density, as reported in the literature [41 - 43].

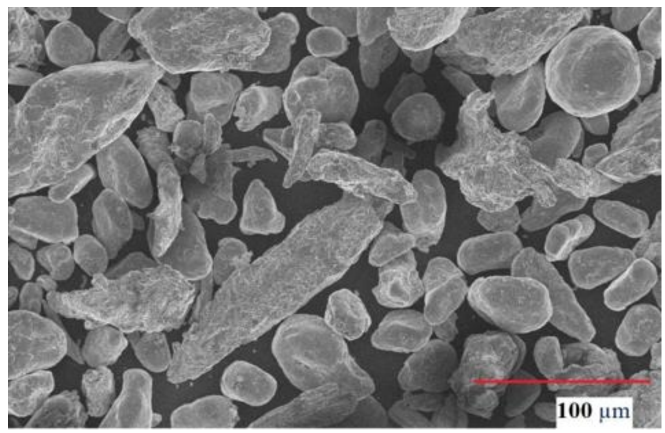

Fig. 1 SEM images of the iron powder

Chemical composition of the powder is determined using the Spark Emission Spectroscopy method (Thermofisher Scientific Spark Spectrometer, Pune, India, Model number: ARL 3460). The iron powder has more than 99.8 % purity with the following specific impurities:

- Carbon: 200 ppm
- Sulphur: 50 ppm
- Phosphorus: 50 ppm
- Lead: 10 ppm
- Oxygen and Oxides: 100 ppm

2.1. Controlled Environment Annealing of the Iron Powder

The Fe74 powder was subjected to controlled environment annealing to improve its magnetic properties. Annealing was carried out at 550 °C for 45 minutes in a cracked ammonia atmosphere, followed by slow furnace cooling. The annealing was performed at this temperature to ensure effective reduction of the powder while avoiding excessive sintering or neck formation between particles. The annealing treatment also relieves deformation-induced residual stresses introduced during the ball-milling operation, which is beneficial for the iron powder magnetic permeability improvement. The reducing atmosphere at higher temperature reduces oxide layer on the powder particles while avoiding additional surface oxidation. Slow furnace cooling of the powder further helps to minimize the development of thermal stresses and preserves the stress-relieved condition prior to compaction. The selected annealing temperature and furnace holding time was selected to ensure necessary powder flowability and particle discreteness, while avoiding the formation of hard agglomerates or lumping that may occur at higher annealing temperatures. This controlled environment heat treatment ensures reduction of the powder and improvement in the magnetic properties, without affecting the handling and compaction behavior.

2.2. Sample Preparation by Compaction and Sintering

The Fe74 powder is used for disc-shaped compacts with a 11 cm outer diameter, 8.9 cm inner diameter, and 0.3 cm thickness. The dimensions of the toroidal specimen were selected to provide sufficient winding space for the primary and secondary coils required for DC magnetic characterization. It is possible to wind large number of turns for relatively bigger sized specimen, that can provide higher value of input magnetization intensity. In the present study, 150 number of primary winding turns provide maximum magnetization intensity up to 10 kA/m. Further, 180 number of secondary coil turns provide necessory sensitivity to determine magnetic flux density in the toroidal specimen, by facilitating measurement of induced voltage in the secondary coil. A smaller sized toroidal specimen has limitations in putting maximum primary and secondary coil turns, limiting the capability to generate higher magnetization intensity and ensuring the required sensitivity of detecting magnetic flux in the toroidal specimen.

The Fe74 powder was mixed with 0.5% (by weight) zinc stearate, which acted as a lubricant. The mixture is used to initially prepare green compacts of 11 cm outer diameter and 0.3 cm thickness, by applying 800 MPa pressure using a 800 Ton capacity press. The green compact samples had a mass of 201.83 g with green densities ranging from 87% to 92%, as determined using the Archimedes water-immersion test. Further, in the next step, the samples were de-lubricated by heating in a nitrogen environment at 450 °C.

The green and de-lubricated specimens, as achieved after compaction, were carefully machined using water jet machining to create 8.9 cm size central hole. Thus, finally, a toroid shaped specimen with outer diameter of 11.0 cm, 8.9 cm inner diameter, and 0.3 cm thickness were prepared to facilitate magnetic characterization. Later, the green compacts were subjected to sintering operation for making hard and mechanically strong specimen. The green compacts were heated at 1000°C temperature in a nitrogen environment during the sintering process. The heating rate during the sintering process was adjusted to get a temperature increase of 30°C /min, and holding time was 30 minutes. Controlled nitrogen environment protects the Fe74 powder particles from oxidation during sintering, thereby facilitating better diffusion bonding and neck formation between adjacent particles. Later, the specimens were cooled down to room temperature by maintaining the cooling rate of 30°C/min. Density of the final sintered specimen was 7.1g/cm3 as determined by the Archimedes water-immersion method. Considering the theoretical density of fully dense pure iron of 7.87 g/cm³, the relative density of the compact was 90.2%, corresponding to an estimated residual porosity of 9.8%. Photograph of the hard sintered toroid specimen is given in Figure 2.

Fig. 2 Toroid shaped specimen photograph after hard sintering

The specimen manufactured using the above route of green compaction, machining and high temperature sintering of the Fe74 powder is hereafter referred as Sintered Pure Iron Powder Compacts.

2.3. Microstructure and Chemical Composition Analysis

EDS and SEM analysis were carried out at the Physics Department in Savitribai Phule Pune University (SPPU), using a Zeiss Sigma HV model. Investigations were conducted on the Fe74 powder, before and after annealing, as well as on the hot-sintered compacts. Figures 3 (a)-(d) shows SEM images for different resolutions of the Fe74 powder before performing the annealing operation.

The size of the particles varies from 30 to 150 µm, with most of them in the range of 60 to 90 µm, which agrees with the reported median particle size of 74 µm. The low-resolution images given in Figures 3(a) and 3(b) reveal that the powder particles were irregular to sub angular agglomerates, with several locally flattened faces and faceted surfaces. The secondary scale-like layer is visible in high-resolution images as a shallow surface texture, as shown in Figures 3(c) and 3(d).

The morphology of these particles is not spherical, and they have surface layers with deformation marks. These surface features are evident due to mechanically induced plastic deformation during the ball milling process, used for manufacturing the powder. These observations are in close agreement with previous results obtained with iron powders produced by mechanical ball milling processes [44, 45]. Figures 4(a) and 4(b) show the SEM results of the iron powder particles after the annealing operation.

The comparison between non-annealed and annealed powder results highlights transformation of the powder surface to a smoother and more uniform surface morphology during the annealing operation. It can be noted that the non-annealed powder has scale-like textures and deformation-induced features, which are not observed in the annealed powder, resulting in a significant reduction in the surface roughness.

Thus, the controlled environment annealing ensures surface stress relieving, microstructure stabilization and uniformity, and a more homogeneous powder surface. Further, the EDS analysis shown in Figure 5 confirms the high purity of the iron powder, with no detectable oxygen or other elemental impurities.

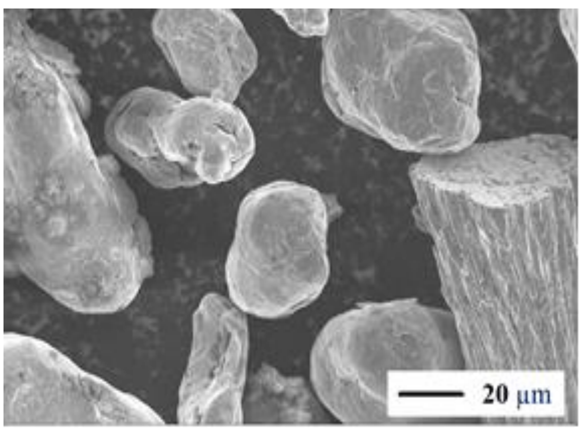

(a)

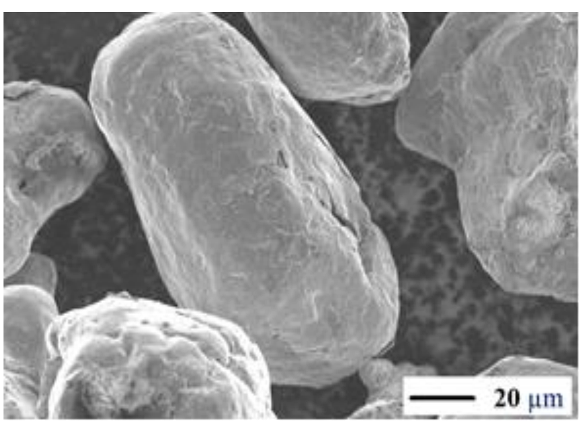

(b)

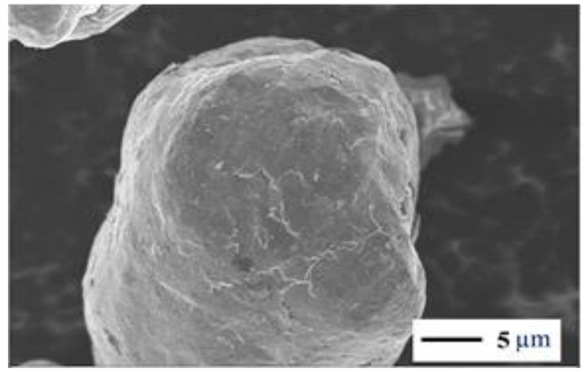

(c)

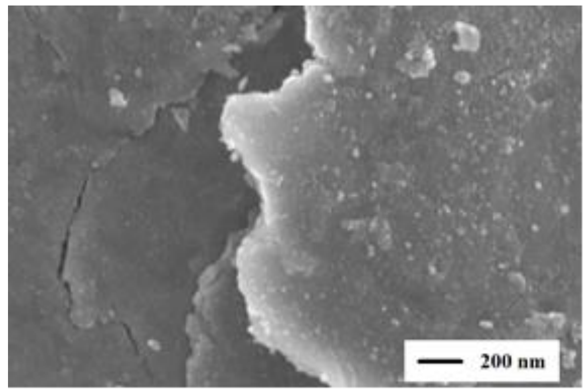

(d)

Fig. 3 (a)-(d) SEM images for non-annealed powder.

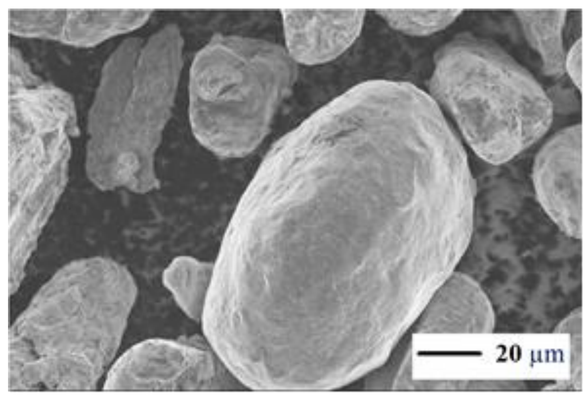

(a)

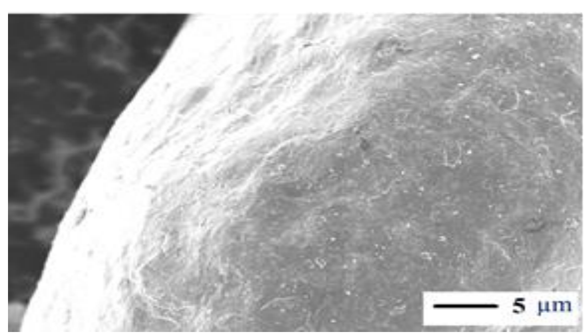

(b)

Fig. 4 (a), and (b) SEM images for the annealed powder.

Figures 6(a)-(d) shows the microstructure of the sintered pure iron compacts. SEM analysis at lower resolution, shown in Figures 6(a) and 6(b), reveals the effect of irregular-shaped iron powder particles with rough surfaces. The particle size distribution and irregular morphology of the Fe74 powder significantly influence the final sintered microstructure, resulting in the non-uniform grain size and interparticle interlocking. The sintered microstructure largely inherits the geometrical characteristics of the powder, which reveals irregular-shaped grains and grain clusters. The characteristic dimensions of the grains in the sintered microstructure are comparable to the initial powder particle size.

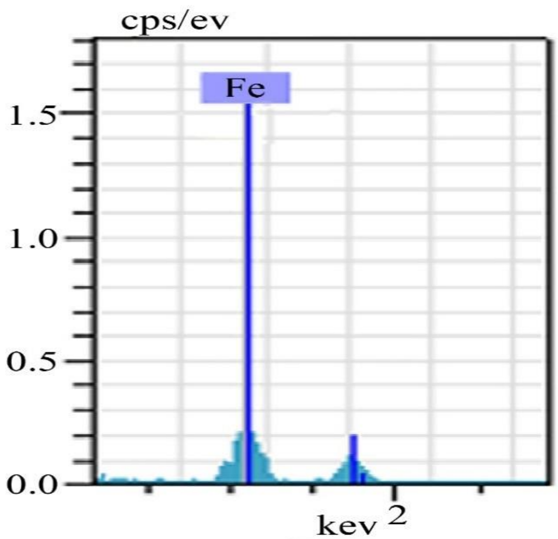

Fig. 5 EDS results for chemical composition

High-resolution SEM images in Figures 6(c) and 6(d) reveal that the hot-sintered compact retains the irregular and angular morphology of the initial iron powder particles. Images reveal interparticle neck formation and particle coalescence, with the particle boundaries having local discernible. The contact regions between neighboring particles were well consolidated, which highlights metallurgical bonding during the sintering process, leading to particle diffusion.

Figure 6(d) shows residual porosity characterized by irregular to sub-rounded pores, which are non-uniformly distributed. Further, these pores are mainly concentrated along interparticle boundaries and at junctions between adjacent particles.

This non-uniform pore distribution in the sintered specimen is consistent according to the particle size distribution of the initial powder. Microstructure of the sintered specimen indicates that densification and bonding are developed predominantly during the high-temperature sintering stage. The earlier green compaction stage established intimate particle contact and geometric interlocking.

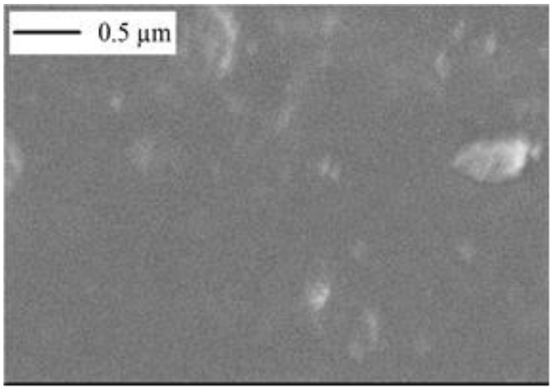

(a)

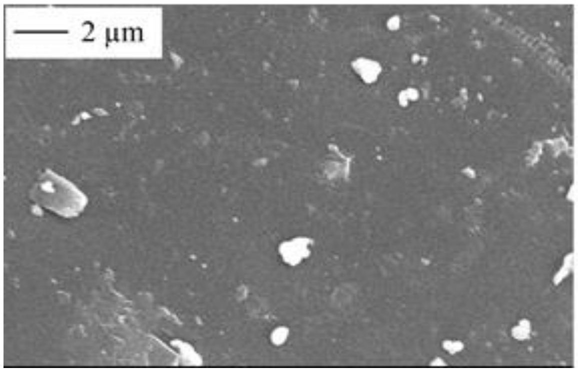

(b)

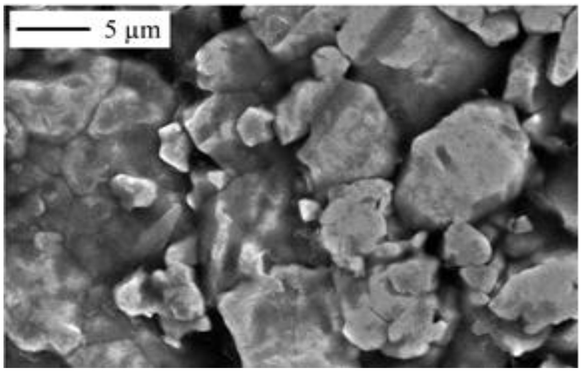

(c)

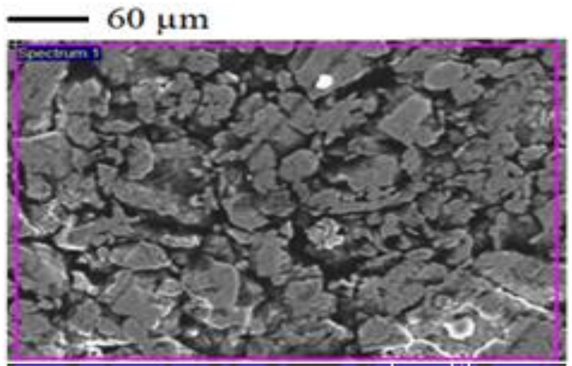

(d)

Fig. 6 (a)-(d) SEM images for sintered specimen.

2.4. Magnetization Characteristics

After manufacturing the toroid shaped samples, important magnetic properties are determined using standard magnetic characterization process. The properties include initial magnetization curve, coercivity, remanence, permeability, and hysteresis loop, which are critical for low frequency magnetic shielding application. The properties determined from the above mentioned experimental investigation are subsequently used for theoretical simulations to evaluate SE for low-frequency magnetic shielding.

2.4.1. Initial Magnetization Curve

The DC magnetic characterization of the material was conducted following the IEC 60404-4 international standard. The experimental testing was performed at the facility in Vishwakarma University, Pune. The measurement system utilized the following specifications:

- Maximum Magnetization Intensity: 10 KA/m
- Maximum Flux Density: 2.0 T
- Measurement Accuracy: 0.5 %
- Measurement Method: Ring specimen using point-by-point measurement
- Primary Coil Turns: 150
- Secondary Coil Turns: 180
- Power Source: Voltage-controlled current source

In the characterization process, primary and secondary windings were evenly distributed over the specimen. The primary coil was connected to the controlled current DC power supply, and the voltage across the secondary coil was measured to estimate the toroidal specimen magnetic flux density. The intensity of the magnetic field was raised from zero to maximum limit by increasing the input DC current to the primary coil. Care was taken to give sufficient time so that the magnetic field in the specimen is getting stabilized, during the measurement process. Point to point measurement approach, as per IEC60404-4 is followed for the DC magnetic characterization. Each of the data points is recorded after stabilization of the magnetic field for the corresponding magnetization intensity, with the system measurement accuracy of ± 0.5%. The individual measurement data points are reported in Figures 7 - 9.

The reported curves represent the measured magnetic response of the investigated specimen, while specimen-to-specimen variability remains outside the scope of the present study, since only two ring specimens were prepared in the present study. The initial magnetization curve for the sintered pure iron powder compact is shown in Figure 7, which is further used to determine the relative magnetic permeability variation, as reported in Figure 8. The maximum magnetic permeability of the specimen was 6300. It can also be noted that magnetic saturation is not observed within the limits of the applied magnetization intensity, due to the fact that flux density saturation limit for the pure iron material is much higher in comparison to the maximum flux density applied in the present experimental set up. Hysteresis loop for the sintered pure iron compact is plotted as per the guidelines of IEC 60404-4 standard and is shown in Figure 9. Important parameters of the hysteresis loop and the initial magnetization curve are as follows.

i. Remnant flux density- 1.0 T
ii. Coercivity- 70 A/m
iii. Maximum flux density- 1.4 T

The initial magnetization curve for the proposed material reported in Figure 7 is used for theoretical simulation to determine low frequency SE, and is discussed in the further sections.

2.5. Finite Element Analysis for Magnetic Shielding

The use of pure iron powder compacts for low frequency electromagnetic shielding is discussed in this section. The shielding material is used for attenuation of low frequency magnetic field generated around a DC current carrying conductor. Finite Element Analysis (FEA) is performed to determine SE, and results are compared to substitute materials, including Fe-Si electrical steel (ASTM 30F677) and Mu-metal (ASTM A754 alloy). Present study focusses on DC magnetic shielding; therefore, magnetostatic FEA is carried out using the two-dimensional electromagnetic model in ANSYS-18.2. The conductor is located in the center, and the shielding material is wrapped around. The shielding material is used in different configurations and materials.

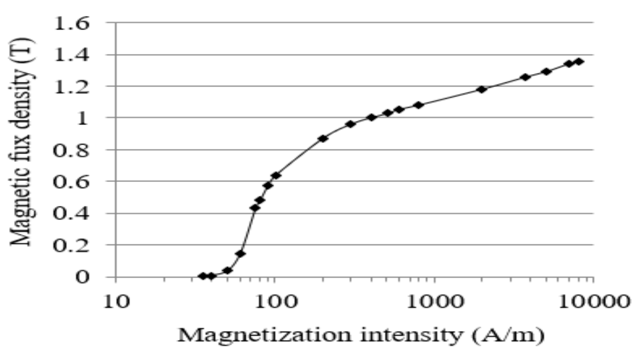

Fig. 7 Initial magnetization curve

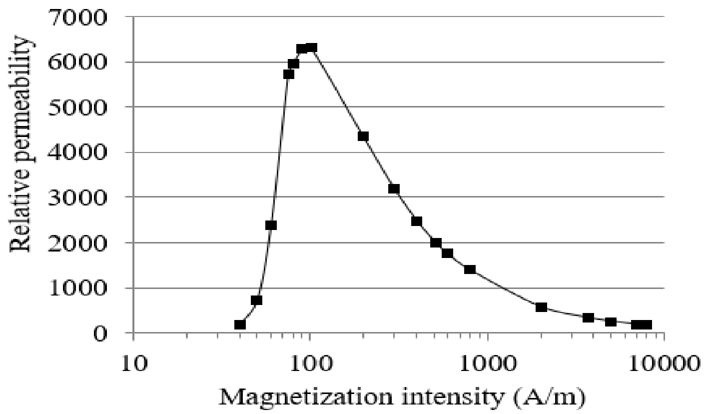

Fig. 8 Variation of permeability

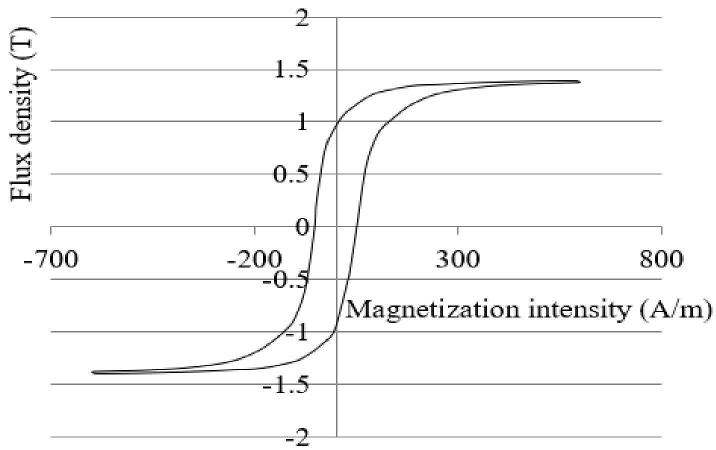

Fig. 9 Hysteresis loop

The geometries defined in the FEA consist of conductor material, air and shielding material. Following are the assumptions in the FEA simulation;

- The conductor is infinitely long and represented using a two-dimensional cross-section.
- The conductor is positioned at the center of the shielding geometry.
- The shielding material is homogeneous and isotropic, and contact gaps, joints, manufacturing defects, and local material properties variations are neglected.
- Temperature effects on magnetic properties are neglected.

Following shielding geometries are investigated in the present study:

- Open Shunt Geometry: Two plates are located at the top and bottom position of the conductor at a distance of 150 mm, as shown in Figure 10(a).
- Closed Shunting Geometries: Square, hexagonal, and circular shapes are modeled around the conductor at a 150 mm radial distance as illustrated in Figures 10(b), 10(c), and 10(d).

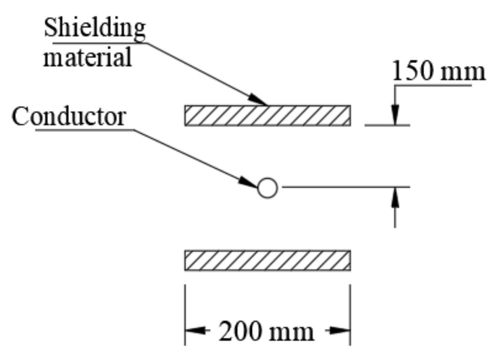

(a)

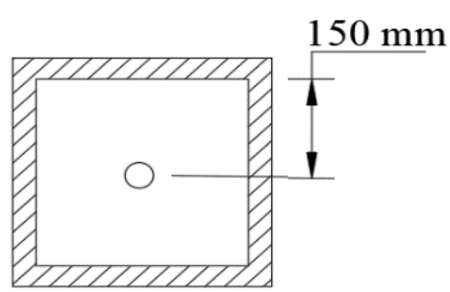

(b)

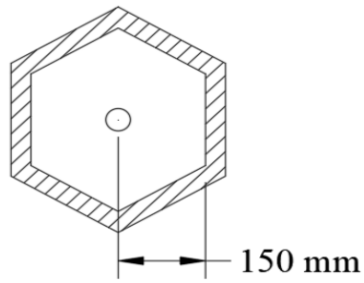

(c)

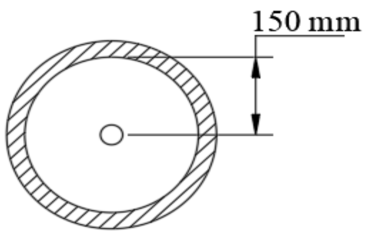

(d)

Fig. 10 (a) Open shunting geometry, (b) Square shielding geometry, (c) Hexagonal shielding geometry, and (d) Circular shielding geometry.

The diameter of the conductor is 20 mm, and 1000 Amp current is passed through the conductor during the FEA simulation. The dimensions and current value used in the simulation were selected as representative of high-current power-cable shielding applications [46]. Parameters in the FEA simulation are reported in Table 1. The surrounding air region is defined as an outer radius of 500 mm with INFIN110 infinite-boundary elements applied at the outer edge to represent an unbounded air region. Use of this element reduces artificial field truncation effects.

A non-uniform meshing approach is followed with finer mesh size near the conductor and within the shielding material, while coarse meshing is used in the surrounding air. Fine mesh at the region of interest facilitates accurate estimation of the magnetic flux gradient. The mesh size is gradually coarsened in the surrounding area where the magnetic field variation is comparatively lower. Outermost boundary is applied with zero vector potential, and current density is applied at the conductor as the excitation. The current density is calculated based on the applied DC current of 1000 A along the 20 mm diameter conductor.

The spacing between the conductor and the shielding material, along with the dimensions of the magnetic shield, significantly influences magnetic flux shielding performance. In the present study, the shielding is placed at radial distances as illustrated in Figures 10(b)-10(d), which are selected based on the typical space available around underground and overhead cables.

Table 1. Parameters used for FEA

S. No.	Component and properties	Ansys element
1	Air- Relative permeability(μ_{per} = 1.0)	Plane 233 Infin 110 at Boundary
2	Copper conductor-Relative permeability and Electrical resistivity (μ_{per} = 1.0,resistivity - 1.68×10^{-8} Ω·m)	
3	Shielding material- B-H curve (for sintered pure iron compacts - determined in Section 3 andreported in Figure 7, for Mu- metal- [47], Fe-Si steel- [48])	
4	Conducting material-Relative permeability and Electrical resistivity (μ_{per} = 1.0,resistivity: 1.68×10^{-8} Ω·m)	

3. Results and Discussion

The electromagnetic shielding is applied around the current-carrying conductor so that the magnetic field intensity around the conductor can be reduced to a safe level. Effectiveness of the magnetic shielding is determined by using the following formula;

$$SE = 20 \log_{10} (B_0/B_s) \quad (1)$$

Where B0 is maximum magnetic flux density at 1 m radial distance from the conductor without using a magnetic shield, and Bs is the maximum magnetic flux density at 1 m radial distance from the conductor with using the magnetic shield. FEA simulation is carried out to find out the magnetic flux density around the conductor. Figure 11 shows magnetic flux density variation around the conductor without using magnetic shielding, and the flux lines are shown in Figure 12. In addition, FEA simulations are performed using various type of shielding materials with different geometries and shielding material thickness, and is discussed further.

Figures 13-16 show flux density variation around the conductor for open, square, hexagonal, and circular geometries with a shielding material thickness of 3.5 mm. Results shown in Figures 13-16 reveal that maximum flux density inside the shielding material in the case of these geometries are 3.0 mT, 1.28 mT, 0.138 T, and 1.19 T, respectively.

In the case of the shielding material with a lower reluctance path, the shielding material pulls maximum flux lines within itself, ensuring a higher flux density in the shielding material. The magnetic flux density distribution within the shielding material was strongly influenced by the shield geometry. In case of the open geometry, the flux density values varied from 0.7 to 3 mT, whereas the square geometry exhibited slightly lower variation from 0.59 to 1.28 mT. There was a variation from 0.022 T to 0.138 T for the hexagonal geometry. Variation of the flux density within the shielding material indicates a non-uniform magnetic field distribution within the shielding material. However, the circular geometry ensured a constant magnetic flux density of 1.19 T in the shielding material. This uniform distribution is achieved due to smooth magnetic path provided by the circular geometry. On the other hand, openings and geometric discontinuities in the other configurations lead to localized flux redistribution and higher magnetic flux density variation. Figures 17 and 18 shows magnetic field lines around the conductor for open and circular geometries. Magnetic flux density value at radial distance of 1.0 m is determined using the FEA. Figure 19 reports values of maximum flux density at 1.0 m distance from the conductor, for different shielding geometries and thickness, when using the proposed pure iron sintered material used for magnetic shielding. The DC magnetic flux shielding is ensured primarily by the higher permeable sintered pure iron material. It is evident from Figure 19 that among the different shielding geometries, closed shielding geometries perform better to achieve higher SE than other geometries. In case of open geometry, there is higher flux leakage from the shielding geometry due to gaps in the flux flow path, which is evident in Figure 17. On the other hand, closed geometries have least leakage flux, leading to better SE. Further, among the closed geometries, circular configuration makes it more effective than square and hexagonal shapes, as shown in Figure 16. Closed geometries have a continuous low reluctance path to the magnetic flux lines, which results in lower magnetic flux density at 1 m distance, and hence higher SE. This will make sure the flux lines are deflected into the shielding material and run in the closed path. In case of circular geometry, the magnetic path reluctance is lowest due to absence of bends in the flow path.

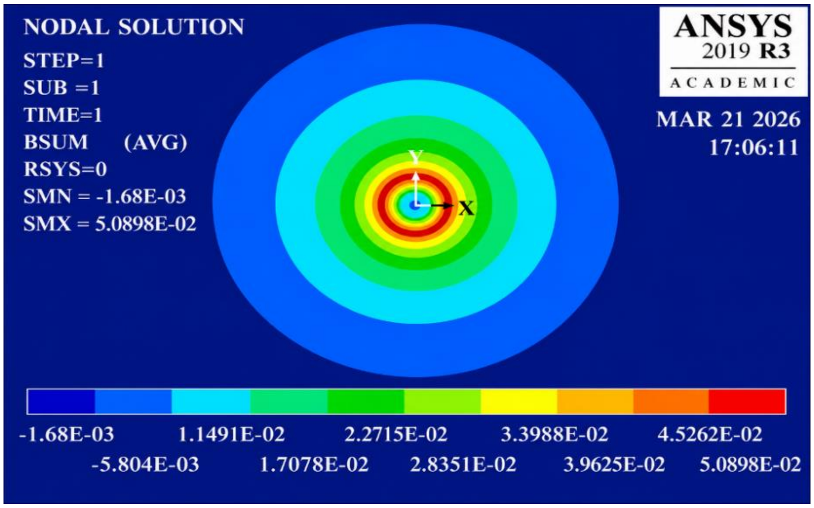

Fig. 11 Magnetic flux density around the conductor

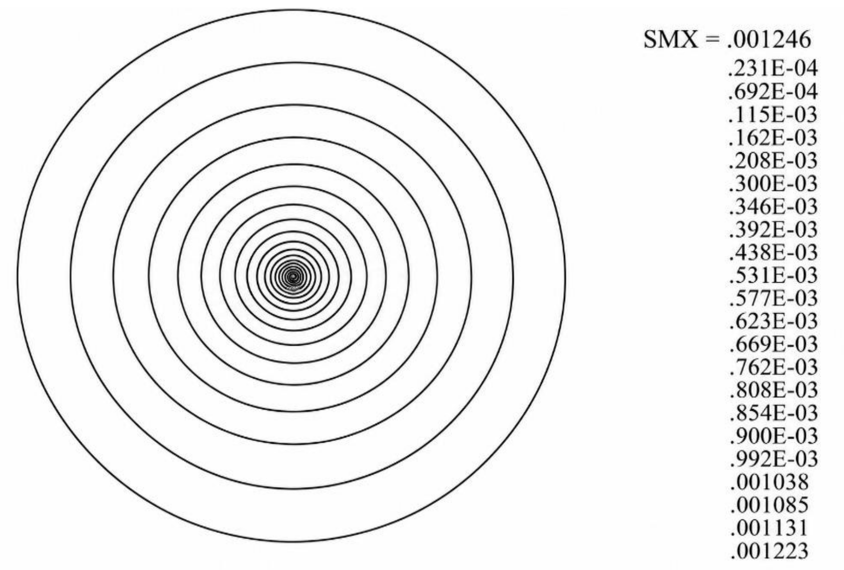

Fig. 12 Magnetic flux lines around the conductor

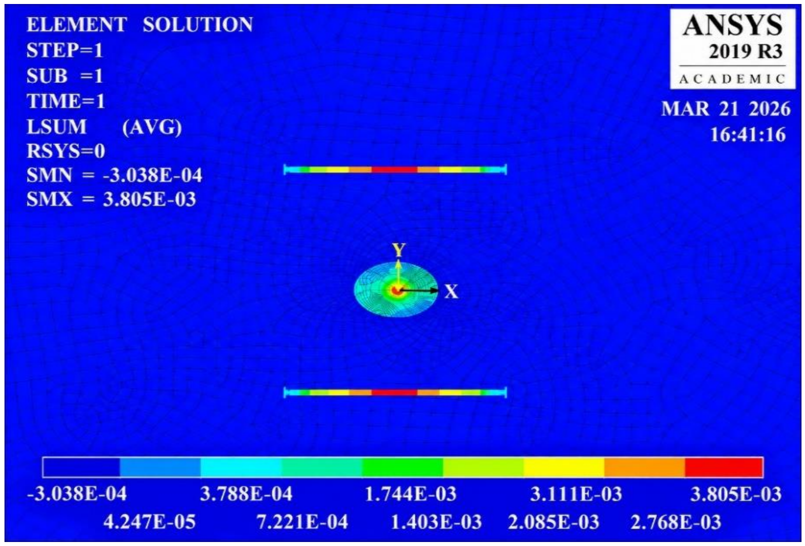

Fig. 13 Magnetic flux density for open shielding geometry

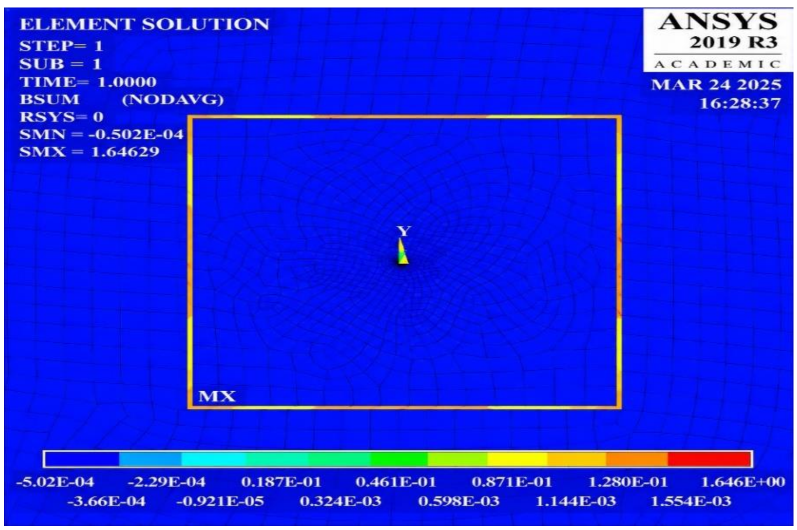

Fig. 14 Magnetic flux density around the conductor for square shielding geometry

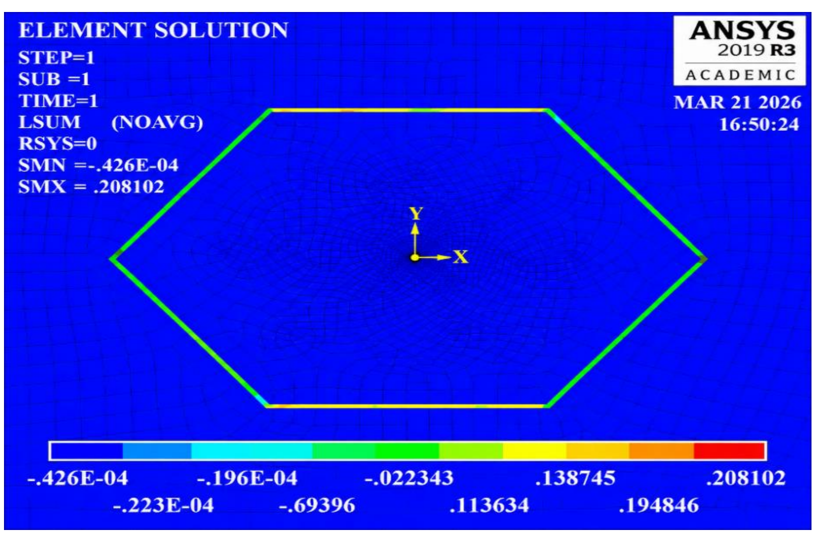

Fig. 15 Magnetic flux density around the conductor for a hexagonal shielding geometry

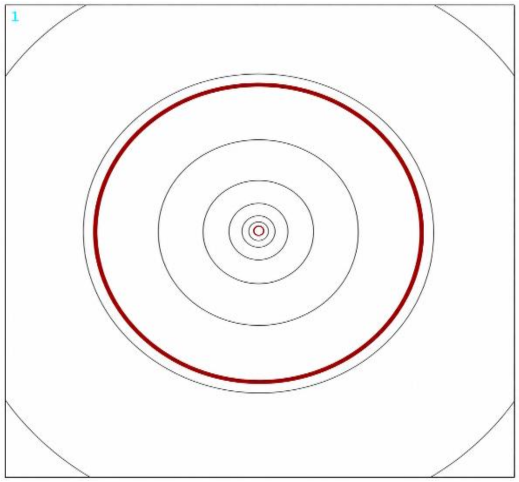

Fig. 16 Magnetic flux density around the conductor for circular shielding geometry

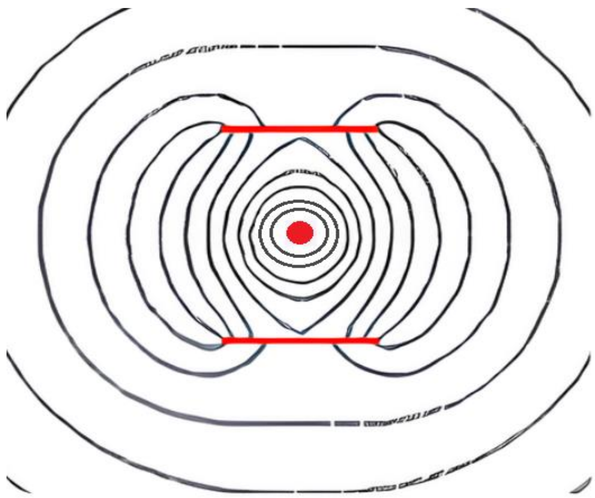

Fig. 17 Magnetic flux lines around the conductor for open shielding geometry

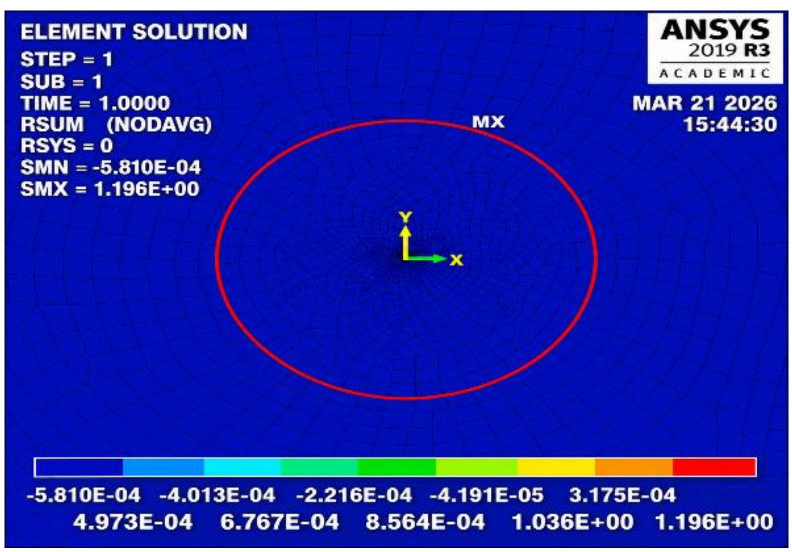

Fig. 18 Magnetic flux lines around the conductor for circular shielding geometry

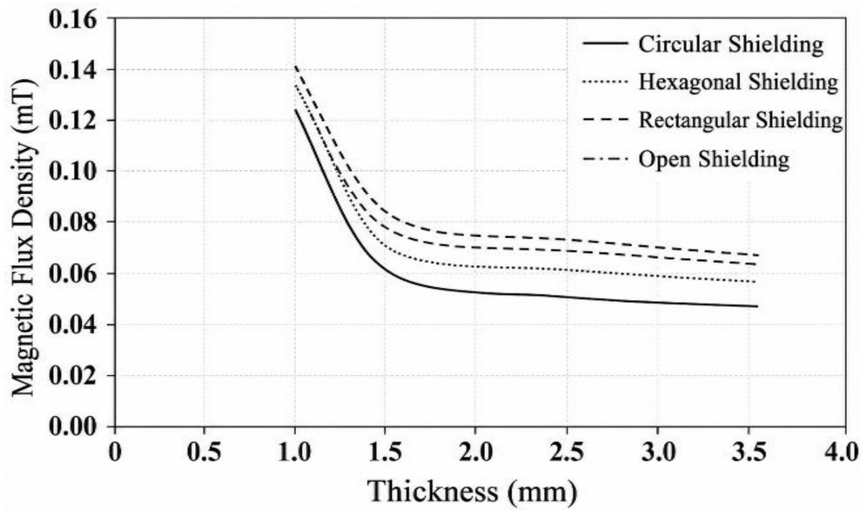

Fig. 19 Variation of maximum magnetic flux density at 1.0 m for different shielding geometries and shielding thickness

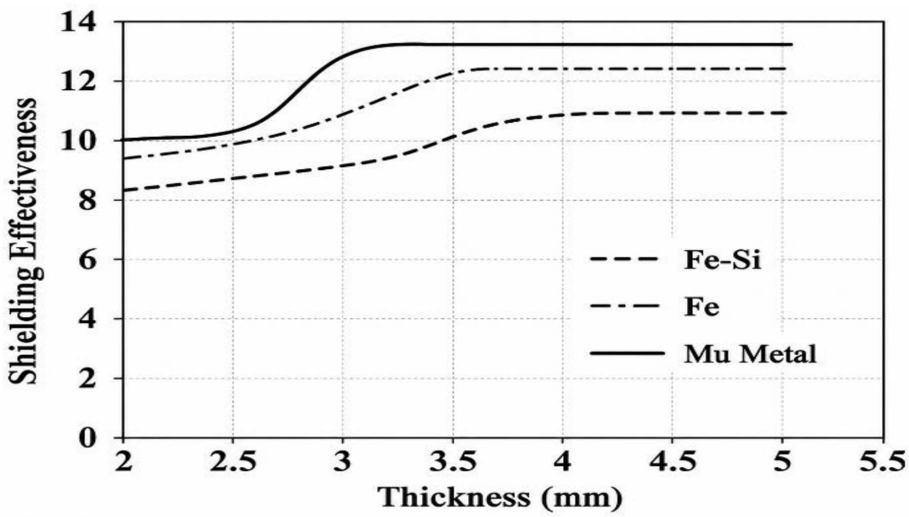

Fig. 20 Variation of SE for different shielding materials and shielding thickness

On the other hand, hexagonal and square geometries have 6 and 4 bend locations, respectively, in the magnetic flux flow path. Number of bends in the flow path results in flux crowding and increases resistance to magnetic flux flow. This results in reduction in the magnetic flux line in the shielding geometry and increased magnetic flux density around the conductor. Hence, the SE is greater in circular geometry than hexagonal, square and open geometries. After validating most suitable geometry for shielding, simulations are performed using the circular shielding geometry to determine the magnetic flux density at 1.0 m distance when using different shielding materials with varying thickness. Further, the flux density values are used to calculate SE, and the results are reported in Figure 20.

It can be noted from Figure 20 that Fe-Si steel gives a maximum SE of 11.24 dB for a shielding thickness of 4.2 mm. In the case of Mu-metal, a maximum SE of 13.35 dB can be achieved with 3 mm shielding material thickness. The proposed pure iron sintered material shield will ensure 12.6 dB of SE for a 3.5 mm thickness. Mu-metal gives higher SE due to greater magnetic permeability.

For DC and low-frequency applications, thicker shielding results in redirecting a large portion of the magnetic flux lines inside the shielding material. Redirecting larger flux lines in the material reduces the surrounding magnetic flux density, resulting in an improvement in the SE. In case of the given input magnetic field, there is a critical value of the thickness, beyond which no further improvement in the SE is obtained, even if the shielding material thickness is increased. This happens due to magnetic saturation, where the material cannot take more flux lines and has a limit of maximum magnetic field that it can redirect into itself, such that this saturation limit is the material property. Therefore, for the given input magnetic field, there exists a critical value for shielding thickness in case of the given material. Beyond this critical thickness, there is no improvement in the SE, even if the thickness is increased. On the other hand, thicker material will increase weight and cost. It can be noted from Figure 20 that the critical shielding thicknesses for Mu metal, Fe-Si electrical steel and pure iron materials are 3.0 mm, 3.5 mm, and 4.2 mm, respectively.

Sintered pure iron compacts prepared in the present study have an estimated residual porosity of 9.8%, based on the measured density of 7.1 g/cm³ relative to the density of fully dense pure iron. The presence of porosity can reduce magnetic permeability due to the possible interruption in the magnetic flux continuity. However, magnetic properties characterization revealed that the investigated compact has a maximum relative permeability of 6300 and can achieve a maximum SE of 12.6 dB. During performing FEA, the effect of residual porosity was considered by using the experimentally measured nonlinear B-H curve of the manufactured prototype sintered specimen. This approach is different than estimating the B-H curve by comparing the manufactured material with that of the fully dense iron. During manufacturing compacts, controlled-environment annealing reduced deformation-induced internal stresses, ensuring improved permeability, while high-pressure compaction and sintering resulted in better particle contact, interparticle neck formation, density, which leads to better magnetic-flux continuity. Furthermore, possibility of achieving near-net-shape manufacturing will minimize subsequent cold or hot deformation, which may otherwise have adverse effect on the magnetic properties due to residual stresses and plastic deformation. Therefore, it can be concluded that although the proposed sintered material has slightly lower density than fully dense iron, the sintered compact can demonstrate a competitive magnetic shielding performance because of its high purity, improved magnetic properties, higher saturation capability, and geometry flexibility.

FEA analysis indicates that the shielding material proposed in the present study reduces the magnetic flux density from 0.2 mT to 0.042 mT, corresponding to a 79% reduction in the magnetic field around the conductor. FEA simulation reveals that the maximum magnetic flux density with circular geometry shielding at 1 m and 2 m distances from the current-carrying conductor will be 43 µT and 19.9 µT, respectively. According to the International Commission on Non-Ionizing Radiation Protection (ICNIRP), the exposure limit for the general public for static magnetic fields is 400 mT [49].

The resulting magnetic flux density values at 1 m and 2 m from the conductor are therefore substantially below this limit. Therefore, the proposed shielding provides a significant reduction in external magnetic-field exposure and increases the compliance margin relative to internationally accepted health-protection guidelines.

The proposed sintered pure-iron powder compact provides sustainability advantages in addition to magnetic shielding performance, as follows,

- The material uses pure iron as the principal constituent, which is widely available, recyclable, and easier to process compared with complex Ni-rich high-permeability alloys. Economical material and processing cost. Further, the shieling geometry can be repaired and recycled easily.
- The powder-compaction and sintering route ensures near-net-shape fabrication, which significantly reduces machining waste and facilitates the shielding geometry manufacturing in the required shape and size. For low-frequency shielding applications (DC to < 1kHz), the proposed material has advantages since it can be fabricated with the required thickness (up to 20 mm) into custom geometries. This frequency range covers various applications, including motors, pumps, power electronics housing, medical instruments, sensors, and EV modules. For the low-frequency application, comparatively lower resistivity of the pure iron-based material does not adversely affect the shielding performance. This overcomes limitations of the other substitute materials, which are typically available in standard shapes, including flat sheets and thin ribbons, which are difficult to fabricate for complex geometries and higher thickness. Further, a higher value of saturation flux density of the pure iron compacts enables it to withstand higher stray magnetic field intensity.
- The shielding-thickness study using finite element analysis helps to determine the critical thickness beyond which further increase in material does not significantly improve SE, avoiding unnecessary material use, weight, and cost.
- The developed shield can be used around high-current conductors and low-frequency sensors to reduce magnetic-field exposure, improve measurement reliability, and extend the useful life of sensing systems. These aspects make the proposed material relevant to sustainable industrial infrastructure, responsible material use, and safer electrified environments.
- The sintered pure iron powder compact material can be used in a hybrid configuration along with a conducting layer for medium to high frequency electromagnetic attenuation. This hybrid design enables permeability governed shielding at low frequencies and conductivity governed electromagnetic shielding at higher frequencies. This will ensure application of the iron powder compacts over a broad frequency range.

The present study evaluates the application of the sintered pure iron material for use in magnetic shielding, when placed around a current-carrying conductor, where homogeneous and isotropic properties are used in the two-dimensional magnetostatic FEA. The experimental data obtained after magnetic characterization are used in the analysis, which has enabled the systematic assessment of the shielding performance of the proposed material. The present two-dimensional model does not include three-dimensional end leakage, joints, air gaps, manufacturing tolerances, conductor eccentricity, temperature effects, and material-property variations. In the future, it is proposed to undertake full-scale experimental field validation with three-dimensional geometry and time- as well as frequency-dependent analyses. In order to investigate high-frequency shielding performance, a possible sandwich structure with the sintered pure iron compacts and an electrically conducting layer will be investigated.

The proposed use of a three-dimensional experimental approach in the future will enable the evaluation of joints, openings, mechanical reliability, corrosion resistance, manufacturing cost, and life-cycle performance. In the present study, one final density condition of the sintered pure iron compact was investigated, and the results represent one quantitative porosity–shielding data point in the B-H curve, rather than revealing a general mathematical relationship. Future studies will evaluate multiple compaction and sintering conditions to manufacture the compacts with different density values so that a direct correlation can be established between porosity, permeability, and SE.

4. Conclusion

This paper has proposed a new material for low frequency and DC magnetic shielding applications. The material is manufactured using Fe74 electrolytic pure iron powder, subjected to controlled environment annealing, compaction and sintering. SEM and EDS analysis are performed to investigate the morphology and chemical analysis of the iron powder and that of the sintered specimen. The analysis revealed that the hot-sintered pure iron compacts retained the irregular powder morphology, while there was a diffusion-driven interparticle metallurgical bonding and neck growth, with residual rounded/sub-rounded porosity present along particle boundaries and triple junctions. The DC magnetic characterization was carried out according to IEC 60404-4 standard to determine the initial magnetization curve and important hysteresis parameters. It was revealed that the proposed material has the necessary soft-magnetic characteristics, with a remanent flux density of 1.0 T, coercivity of 70 A/m, maximum flux density of 1.4 T, and maximum permeability of 6300, which makes this material suitable for low-frequency magnetic shielding applications. The magnetic properties determined from the experimentation are further used in performing FEA to investigate SE achieved by using the proposed material in different configurations and thicknesses. The simulation studies indicate that circular geometry shield of the proposed material with 4.2 mm thickness can ensure a maximum SE of 12.6 dB, which was better than Fe-Si shielding material and comparable to Mu-metal. The proposed low frequency shielding material offers a sustainable, economical, and recyclable solution that can be manufactured in near-net-shape. Further, it can be combined with conductive layers, enabling its use in high-frequency shielding for various applications in industrial, EV, sensor, medical, and power-system shielding.

Acknowledgement

The authors gratefully acknowledge the Department of Physics, Savitribai Phule Pune University, for providing access to the Scanning Electron Microscope facility, which was established with financial support from the Department of Science and Technology (DST), Government of India, under the DST-FIST Programme (SR/FST/PS II-003/2000).

References

[1] Xueping Xu et al., “Magnetic Shielding Mechanism and Structure Design of Composites at Low Frequency: A Review,” *Journal of Magnetism and Magnetic Materials*, vol. 570, 2023. [CrossRef] [Google Scholar] [Publisher Link]

[2] S. Geetha et al., “EMI Shielding: Methods and Materials—A Review,” *Journal of Applied Polymer Science*, vol. 112, no. 4, pp. 2073-2086, 2009. [CrossRef] [Google Scholar] [Publisher Link]

[3] Cheng-Hsien Yeh et al., “High-Entropy Alloys as Magnetic Shielding Materials in Low-Frequency Wireless Power Transmission,” *Materials Today Advances*, vol. 24, pp. 1-11, 2024. [CrossRef] [Google Scholar] [Publisher Link]

[4] Shuai Kang et al., “Simulation Research on Low-Frequency Magnetic Noise in Fe-Based Nanocrystalline Magnetic Shields,” *Materials*, vol. 18, no. 2, pp. 1-11, 2025. [CrossRef] [Google Scholar] [Publisher Link]

[5] Yiyi Jing et al., “Low-Frequency Magnetic Shielding of a Double-Layered Planar Shield against a Parallel Loop,” *IEEE Transactions on Electromagnetic Compatibility*, vol. 66, no. 5, pp. 1430-1439, 2024. [CrossRef] [Google Scholar] [Publisher Link]

[6] Bo Li et al., “Additively Manufactured Ni-15Fe-5Mo Permalloy via Selective Laser Melting and Subsequent Annealing for Magnetic-Shielding Structures: Process, Micro-Structural and Soft-Magnetic Characteristics,” *Journal of Magnetism and Magnetic Materials*, vol. 494, 2020. [CrossRef] [Google Scholar] [Publisher Link]

[7] C. Gohil et al., “Measurements of Sub-nT Dynamic Magnetic Field Shielding with Soft Iron and Mu-Metal for Use in Linear Colliders,” *Journal of Instrumentation*, vol. 15, pp. 1-13, 2020. [CrossRef] [Google Scholar] [Publisher Link]

[8] Airu Ji, and Jinji Sun, “A Progressive Loss Decomposition Method for Low-Frequency Shielding of Soft Magnetic Materials,” *Materials*, vol. 17, no. 22, pp. 1-9, 2024. [CrossRef] [Google Scholar] [Publisher Link]

[9] Indranil Chakraborty, Suryasarathi Bose, and Kaushik Chatterjee, "Designer Fe_3O_4@Ag Core–Shell Porous Nanospheres for Enhanced Electromagnetic Interference Shielding of Polymer Nanocomposites," *Advanced Engineering Materials*, vol. 25, no. 8, 2023. [CrossRef] [Google Scholar] [Publisher Link]

[10] Yi-Huan Lee et al., "Lightweight, Highly Efficient, and Recyclable Absorption-Dominated Electromagnetic Interference Shielding Foams based on Molecularly Designed Polyamide Elastomer/Carbon Nanotube Nanocomposites," *ACS Applied Polymer Materials*, vol. 6, no. 12, pp. 7006-7019, 2024. [CrossRef] [Google Scholar] [Publisher Link]

[11] Yuanhang Yu et al., "Environmentally Tough and Stretchable MXene Organohydrogel with Exceptionally Enhanced Electromagnetic Interference Shielding Performances," *Nano-Micro Letters*, vol. 14, pp. 1-15, 2022. [CrossRef] [Google Scholar] [Publisher Link]

[12] Jingcheng Li et al., "In Situ Growth of Fe_3O_4 Nanoparticles in Poly(Arylene Ether Nitrile)/Graphene/Carbon Nanotube Foams for Electromagnetic Interference Shielding," *ACS Applied Nano Materials*, vol. 6, no. 9, pp. 7802-7813, 2023. [CrossRef] [Google Scholar] [Publisher Link]

[13] Xiaoguang Yang et al., "Optimization Design of a Giant Magneto Resistive Effect Based Current Sensor with a Magnetic Shielding," *IEEE Transactions on Applied Superconductivity*, vol. 24, no. 3, pp. 1-4, 2014. [CrossRef] [Google Scholar] [Publisher Link]

[14] S. Francis Ignacious Ruban et al., "Coreless Hall Effect Based Current Sensing Technique with Magnetic Shielding," *International Journal of Advances in Computer and Electronics Engineering*, vol. 2, no. 1, pp. 16-23, 2017. [Google Scholar] [Publisher Link]

[15] Zenghua Liu et al., "Development of a Bidirectional-Excitation Eddy-Current Sensor with Magnetic Shielding: Detection of Subsurface Defects in Stainless Steel," *IEEE Sensors Journal*, vol. 18, no. 15, pp. 6203-6216, 2018. [CrossRef] [Google Scholar] [Publisher Link]

[16] Mehran Mirzaei et al., "Eddy Current Speed Sensor with Magnetic Shielding," *Journal of Magnetism and Magnetic Materials*, vol. 502, 2020. [CrossRef] [Google Scholar] [Publisher Link]

[17] Darko Vasić et al., "Model of Magnetically Shielded Ferrite-Cored Eddy Current Sensor," *Sensors*, vol. 22, no. 1, pp. 1-20, 2022. [CrossRef] [Google Scholar] [Publisher Link]

[18] Deqiang Zhou et al., "Influence of Metallic Shields on Pulsed Eddy Current Sensor for Ferromagnetic Materials Defect Detection," *Sensors and Actuators A: Physical*, vol. 248, pp. 162-172, 2016. [CrossRef] [Google Scholar] [Publisher Link]

[19] Katherine Dang et al., "Magnetic Shielding Concepts for Reaction Wheel Assembly on NASA Europa Clipper Spacecraft," *2020 IEEE International Symposium on Electromagnetic Compatibility & Signal/Power Integrity (EMCSI)*, Reno, NV, USA, pp. 305-311, 2020. [CrossRef] [Google Scholar] [Publisher Link]

[20] Ruiqi Zhu et al., "Anisotropic Magnetic Liquid Metal Film for Wearable Wireless Electromagnetic Sensing and Smart Electromagnetic Interference Shielding," *Nano Energy*, vol. 92, 2022. [CrossRef] [Google Scholar] [Publisher Link]

[21] Xin Hou et al., "Enhancing Electromagnetic Shielding Property and Absorption Coefficients via Constructing Electromagnetic Rings in Janus Composites," *Composites Science and Technology*, vol. 257, 2024. [CrossRef] [Google Scholar] [Publisher Link]

[22] Jorge Victoria et al., "Design Approach for High Efficiency NFC Systems with Magnetic Shielding Materials," *2020 International Symposium on Electromagnetic Compatibility - EMC EUROPE*, Rome, Italy, pp. 1-7, 2020. [CrossRef] [Google Scholar] [Publisher Link]

[23] Jaehoon Yoo, and Sangmin Lee, "Experimental Study on Electromagnetic Shielding Characteristics of a Fe-based Amorphous Soft Magnetic Composite," *Applied Sciences*, vol. 12, no. 12, pp. 1-13, 2022. [CrossRef] [Google Scholar] [Publisher Link]

[24] E. Wodey et al., "A Scalable High-Performance Magnetic Shield for Very Long Baseline Atom Interferometry," *Review of Scientific Instruments*, vol. 91, no. 3, pp. 1-6, 2020. [CrossRef] [Google Scholar] [Publisher Link]

[25] Xueyi Zhang et al., "Study of an Electric Vehicle WPT System with Ring-Series Passive Magnetic Shielding Based on Dual Transmitting Coils," *Progress In Electromagnetics Research M*, vol. 129, pp. 53-64, 2024. [CrossRef] [Google Scholar] [Publisher Link]

[26] Gaojie Han et al., "Cellulose-based Ni-Decorated Graphene Magnetic Film for Electromagnetic Interference Shielding," *Journal of Colloid and Interface Science*, vol. 583, pp. 571-578, 2021. [CrossRef] [Google Scholar] [Publisher Link]

[27] Reza Peymanfar, Ali Ahmadi, and Elnaz Selseleh-Zakerin, "Evaluation of the Size and Medium Effects on the Microwave Absorbing, Magnetic, Electromagnetic Shielding, and Optical Properties using $CuCo_2S_4$ Nanoparticles," *Journal of Alloys and Compounds*, vol. 848, 2020. [CrossRef] [Google Scholar] [Publisher Link]

[28] A.M.A. Henaish et al., "Spectral, Electrical, Magnetic and Radiation Shielding Studies of Mg-doped Ni–Cu–Zn Nanoferrites," *Journal of Materials Science: Materials in Electronics*, vol. 31, no. 22, pp. 20210-20222, 2020. [CrossRef] [Google Scholar] [Publisher Link]

[29] Qian-Ming He et al., "Electric-Magnetic-Dielectric Synergism and Salisbury Screen Effect in Laminated Polymer Composites with Multiwall Carbon Nanotube, Nickel, and Antimony Trioxide for Enhancing Electromagnetic Interference Shielding," *Composites Part A: Applied Science and Manufacturing*, vol. 156, 2022. [CrossRef] [Google Scholar] [Publisher Link]

[30] Shaohong Shi et al., "3D-Printed Carbon-Based Conformal Electromagnetic Interference Shielding Module for Integrated Electronics," *Nano-Micro Letters*, vol. 16, pp. 1-15, 2024. [CrossRef] [Google Scholar] [Publisher Link]

[31] Qinniu Lv et al., "3D Printing of Periodic Porous Metamaterials for Tunable Electromagnetic Shielding Across Broad Frequencies," *Nano-Micro Letters*, vol. 16, pp. 1-20, 2024. [CrossRef] [Google Scholar] [Publisher Link]

[32] Athira Rajan, Sibi Kaithakkal Solaman, and Subodh Ganesanpotti, "Electromagnetic Simulation Integrated Strategy to Metamorphose Commercial Cotton into Multifunctional Electromagnetic Interference Shielding Fabrics," *Advanced Composites and Hybrid Materials*, vol. 8, no. 2, pp. 1-28, 2025. [CrossRef] [Google Scholar] [Publisher Link]
[33] T. Waeckerlé et al., "Evolution and Recent Developments of 80%Ni Permalloys," *Journal of Magnetism and Magnetic Materials*, vol. 505, 2020. [CrossRef] [Google Scholar] [Publisher Link]
[34] Muhammad Ali, and Faiz Ahmad, "A Review of Processing Techniques for Fe-Ni Soft Magnetic Materials," *Materials and Manufacturing Processes*, vol. 34, no. 14, pp. 1580-1604, 2019. [CrossRef] [Google Scholar] [Publisher Link]
[35] Xueping Xu et al., "Efficient Magnetic Shielding by Designing Layered Composite with Nanocrystalline and Permalloy for Weak Magnetic Measurement," *Sensors and Actuators A: Physical*, vol. 375, 2024. [CrossRef] [Google Scholar] [Publisher Link]
[36] Jinji Sun et al., "Measurement and Analysis of Magnetic Properties of Permalloy for Magnetic Shielding Devices under Different Temperature Environments," *Materials*, vol. 16, no. 8, pp. 1-12, 2023. [CrossRef] [Google Scholar] [Publisher Link]
[37] Bin Li et al., "The Preparation of High-Purity Iron (99.987%) Employing a Process of Direct Reduction–Melting Separation–Slag Refining," *Materials*, vol. 13, pp. 1-15, 2020. [CrossRef] [Google Scholar] [Publisher Link]
[38] Yuhua Tan et al., "Research Progress and Trends in Iron Metal Purification Processes," *Industrial & Engineering Chemistry Research*, vol. 62, no. 12, pp. 4817-4830, 2023. [CrossRef] [Google Scholar] [Publisher Link]
[39] R. K. Goyal et al., "Synthesis of Iron Nanopowder and its Nanocomposites with High Electrical Conductivity and Thermal Stability," *Journal of Materials Science & Surface Engineering*, vol. 4, no. 1, pp. 339-341, 2016. [Google Scholar] [Publisher Link]
[40] Liu Chun-quan et al., "Preparation of Electrolytic Iron Powder and its Compression Sintering Properties," *Journal of Iron and Steel Research*, vol. 31, no. 9, pp. 822-829, 2019. [CrossRef] [Google Scholar] [Publisher Link]
[41] Swathi K. Manchili et al., "Sintering of Bimodal Micrometre/Nanometre Iron Powder Compacts – A Master Sintering Curve Approach," *Powder Technology*, vol. 391, pp. 557-568, 2021. [CrossRef] [Google Scholar] [Publisher Link]
[42] Jun-ll Song et al., "Compaction Behavior of Bimodal Iron Nanopowder Agglomerate," *Powder Technology*, vol. 338, pp. 333-341, 2018. [CrossRef] [Google Scholar] [Publisher Link]
[43] Joo Won Oh et al., "Analysis of Compaction and Sintering Behavior of 316L Stainless Steel Nano/Micro Bimodal Powder," *Powder Technology*, vol. 322, pp. 1-8, 2017. [CrossRef] [Google Scholar] [Publisher Link]
[44] C Suryanarayana, E Ivanov, and V.V Boldyrev, "The Science and Technology of Mechanical Alloying," *Materials Science and Engineering: A*. vol. 304, pp. 151-158, 2001. [CrossRef] [Google Scholar] [Publisher Link]
[45] D.R. Amador, and J.M. Torralba, "Morphological and Microstructural Characterisation of Low-Alloying Fe Powder Obtained by Mechanical Attrition," *Journal of Materials Processing Technology*, vol. 143, pp. 776-780, 2003. [CrossRef] [Google Scholar] [Publisher Link]
[46] Juan Carlos del-Pino-López et al., "Magnetic Field Shielding Optimization in Underground Power Cable Duct Banks," *Electric Power Systems Research*, vol. 114, pp. 21-27, 2014. [CrossRef] [Google Scholar] [Publisher Link]
[47] MuMETAL® Technical Data / B-H Curve, Magnetic Shield Corporation, Bensenville, IL, USA. [Online]. Available: https://www.magnetic-shield.com/mumetal-technical-data/
[48] 3% Silicon Steel Core Material (Grain-Oriented Electrical Steel), U.S. Department of Energy, National Energy Technology Laboratory, 2018. [Online]. Available: https://netl.doe.gov/projects/files/3percentSiliconSteelCoreMaterialGrainOrientedElectricalSteel_093018.pdf
[49] International Commission on Non-Ionizing Radiation Protection, "Guidelines on Limits of Exposure to Static Magnetic Fields," *Health Physics*, vol. 96, no. 4, pp. 504-514, 2009. [CrossRef] [Google Scholar] [Publisher Link]